

Supplementary information for “Reconciling seismic structures and Late Cretaceous kimberlite magmatism in northern Alberta”

Yunfeng Chen^{1,2,*}, Yu Jeffrey Gu¹, Larry M Heaman³, Lei Wu⁴, Erdinc Saygin², Shu-Huei Hung⁵

¹*Department of Physics, University of Alberta, Edmonton, AB, Canada, T6G 2E1*

²*Deep Earth Imaging, Future Science Platform, CSIRO, Perth WA, Australia, 6151*

³*Department of Earth and Atmospheric Sciences, University of Alberta, Edmonton, AB, Canada, T6G 2E3*

⁴*School of Earth and Planetary Sciences, Curtin University, Perth, WA, Australia, 6845*

⁵*Department of Geosciences, National Taiwan University, Taipei, Taiwan*

Contents of this file

Text S1-S4
Figures S1 to S7
Table S1

Introduction

The supplementary material summarizes the details of seismic tomography (Text S1 and Figures S1-S4), resolution analysis (Text S2 and Figures S5-S7), plate motion calculation (Text S3) and kimberlite emplacement ages (Text S4 and Table S1).

Text S1. Teleseismic finite-frequency tomography

To image the upper mantle structure beneath the northern Alberta kimberlite province, we integrate data from a recently compiled teleseismic dataset [*Chen et al.*, 2018] and additional 12 stations from northern Alberta to improve the regional data coverage. The combined dataset contains 101 stations from 6 networks. We analyze P-wave travel times from 1566 Mw>5.5 earthquakes, recorded between 2006 and 2015 within a distance range of 30-90 deg, and determine the relative P-wave arrival times between station pairs using the multichannel cross correlation method [*VanDecar & Crosson*,

^corresponding author. Tel.: +61 0421 817 554
Email address: yunfeng1@ualberta.ca (Yunfeng Chen)

1990]. The total numbers of the measured P-wave delay times are 114,666 and 10,305 for frequency ranges of 0.3-2.0 (high) and 0.03-0.125 Hz (low), respectively. Finally, a finite-frequency tomographic inversion is performed based on the travel times [Hung *et al.*, 2004, 2010], which is more accurate than ray-theory based approaches as it properly accounts for the scattering and wave front healing of seismic waves [Hung *et al.*, 2000; Montelli *et al.*, 2004].

The seismic dataset is compiled from a recent regional tomographic study [Chen *et al.*, 2018] and is further supplemented by new data from 12 stations in northern Alberta. This new dataset contains 101 stations from 6 networks including Canadian Rockies and Alberta Network (27 stations, 2006-2015), Canadian National Seismograph Network (12 stations, 2006-2015), Regional Alberta Observatory for Earthquakes Studies Network (13 stations, 2013-2015), Canadian Northeast Experiment (24 stations, 2003-2005), Portable Observatories for Lithospheric Analysis and Research Investigating Seismicity network (4 stations, 2010-2014) and Transportable Array of USArray (21 stations, 2006-2009). This joint network contributes a total of 24,971 frequency dependent travel-time measurements. The resulting travel-time pattern after crustal correction is shown in Figure S1, which shows the transition from late arrival times beneath the Cordillera to early arrival times in the craton (Figure S1).

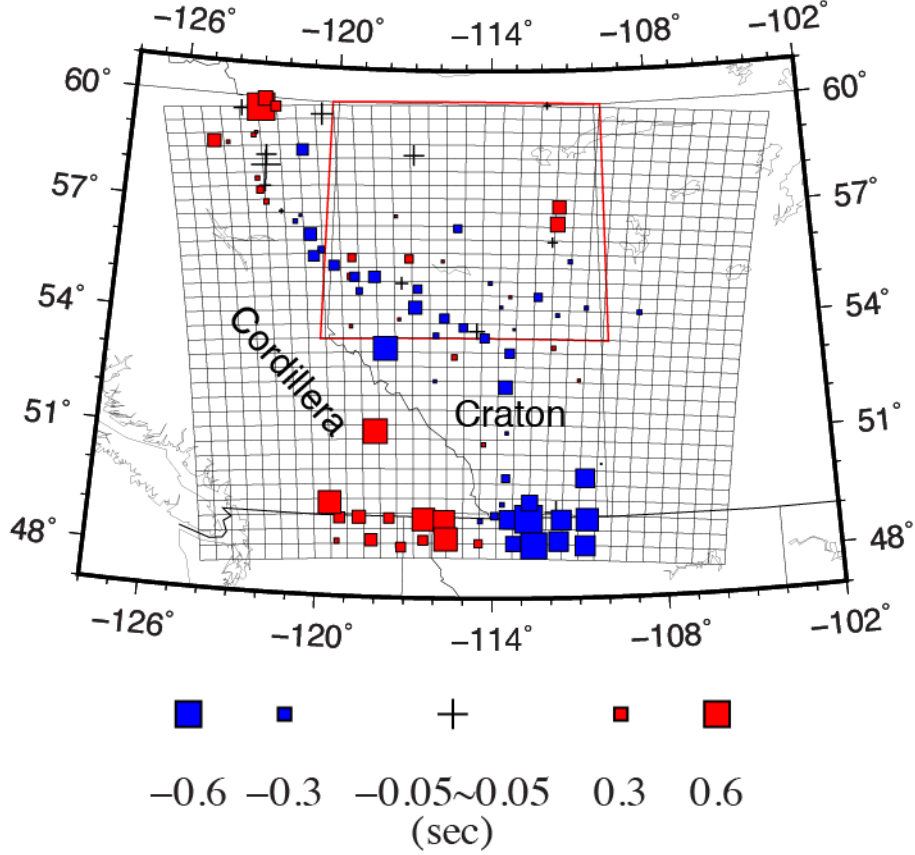


Figure S1. Average travel-time residual at each station. The grid indicates the parametrized model space. The study area of northern Alberta kimberlite province is enclosed by the red rectangle.

The travel time measures are inverted for P-wave velocity via finite-frequency tomography, which is mathematically expressed as

$$\delta t = \iiint_{\oplus} K(\mathbf{x}) \delta s(\mathbf{x}) d^3 \mathbf{x}, \quad (1)$$

where δt is the (demeaned) travel-time perturbations relative to the predicted values based on a reference earth model (AK135; Kennett *et al.*, 1995), $K(\mathbf{x})$ represents the finite-frequency kernel constructed using Born scattering theory and paraxial approximation [Dahlen *et al.*, 2000; Hung *et al.*, 2000], $\delta s(\mathbf{x})$ is the slowness perturbation at location \mathbf{x} and symbol \oplus indicates the 3D integral volume. To solve the slowness term in equation (1) numerically, we parameterize the model space onto a 3D spherical grid with 33 nodes in each dimension (see Figure S1). The model covers a region of $12 \times 12^\circ$ and extends to 800 km depth. The corresponding matrix form of equation (1) is given as

$$\mathbf{d} = \mathbf{G}\mathbf{m}, \quad (2)$$

where \mathbf{d} is the data vector contains M (24,971) relative travel-time residuals and \mathbf{m} is the model vector contains N ($33 \times 33 \times 33 = 35,937$) slowness values. The inversion kernel \mathbf{G} is a $M \times N$ matrix that relates model to data vectors. Equation (2) is typically solved using a damped least-squares scheme as

$$\hat{\mathbf{m}} = (\mathbf{G}^T \mathbf{C}^{-1} \mathbf{G} + \lambda \mathbf{I})^{-1} \mathbf{G}^T \mathbf{C}^{-1} \mathbf{d}, \quad (3)$$

where \mathbf{C} is the covariance derived from measurement uncertainty and \mathbf{I} is the identity matrix and λ is the damping parameter. Instead of solving equation (3) directly, we use a multi-scale parameterization scheme to account for the unbalanced data sampling across the study area. The grid-based model parameterization is transformed into wavelet domain using the hierarchical wavelet decomposition

$$\tilde{\mathbf{m}} = \mathbf{W}\mathbf{m}, \quad (4)$$

where \mathbf{W} is the wavelet transform operator that expands the model slowness vector into wavelet basis and $\tilde{\mathbf{m}}$ is the corresponding wavelet coefficient. The final solution is obtained by applying the inverse wavelet transform as

$$\hat{\mathbf{m}} = \mathbf{W}^{-1} \tilde{\mathbf{m}}, \quad (5)$$

with

$$\tilde{\mathbf{m}} = ((\mathbf{W}^{-1})^T \mathbf{G}^T \mathbf{C}^{-1} \mathbf{G} \mathbf{W}^{-1} + \lambda \mathbf{I})^{-1} (\mathbf{W}^{-1})^T \mathbf{G}^T \mathbf{C}^{-1} \mathbf{d}. \quad (6)$$

The system of linear equations is effectively solved using LSQR algorithm [Paige & Saunders, 1982]. We determine the optimum damping parameter by considering the trade-off between of the variance reduction and L2 model norm (Figure S2). We choose a slightly lower damping value (5000) than that at the turning point (~ 8000) to improve the data fit.

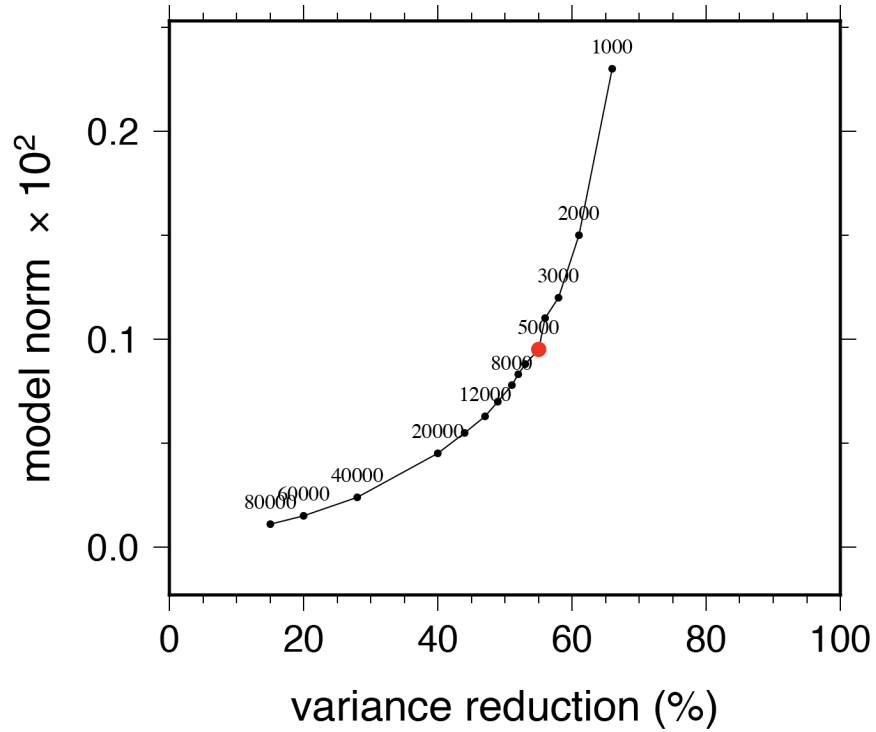


Figure S2. Trade-off curve of variance reduction and model norm. The red circle marks the value used in the inversion.

We examine the data coverage by constructing a ‘hit-count’ map (Figure R3). To this end, we extract the diagonal elements from the resolution matrix (GTG), which provides an intuitive demonstration of the overall sensitivities of P-wave traveltimes to the model space. Contrary to the ray-theory kernel that strictly samples the anomalies along the ray path, the finite-frequency kernel provides volumetric sensitivity surrounding the theoretical ray path. As a result, data sampling is more balanced across the model space, in particular at shallow depths (e.g., above 200 km). In our study area of northern Alberta, the data coverage is reasonable between 54-58° N, whereas the sampling decreases sharply towards the edge of the model. The major velocity anomalies are all observed below 58° N, which increases our confidence in the inversion results.

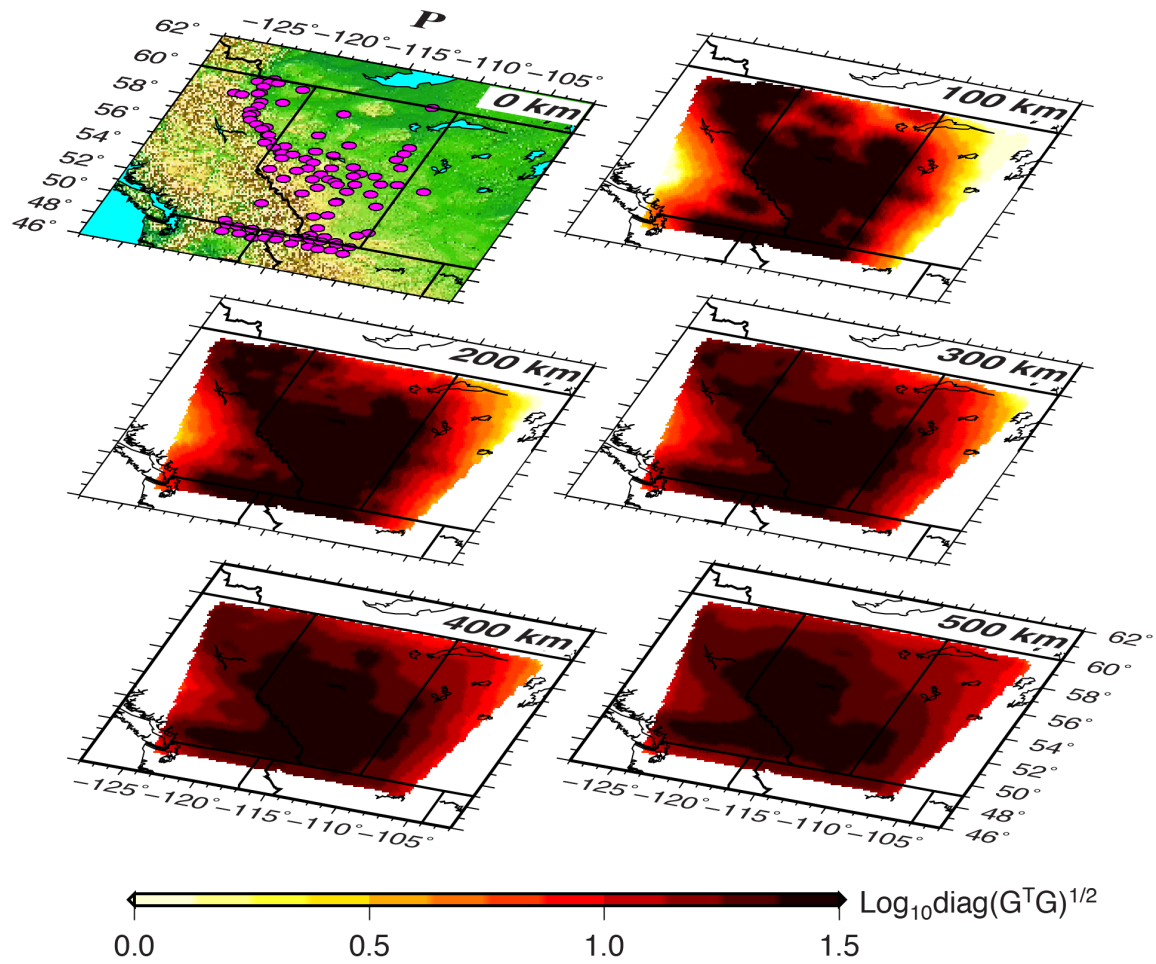


Figure S3. Data coverage at 5 depths revealed by the diagonal elements of the resolution matrix ($G^T G$). The regions with a better data sampling are indicated by darker colors.

Text S2. Resolution analysis

We conduct conventional checkerboard resolution test to analyze the model resolution. The input structures consist of alternating Gaussian shaped velocity anomalies with a maximum absolute amplitude of 3%. Each anomaly spans 7 nodes in three directions, resulting in lateral and vertical dimensions of 250 km and 150 km, respectively, close to the dimension of the major velocity anomalies observed in our study. The synthetic traveltimes are calculated using the actual source-receiver pairs and random noises up with standard deviation of 0.06 sec are added to simulate the real noise level. The inversion is then performed using the same damping parameters and parameterization schemes as those used in the inversion of real data. The degree of recovery of the output ‘checkers’ (Figures S4 (b-d)) compared to the input structures (Figure S4 (a)) offers an

intuitive assessment of the model resolution. The resolution decreases towards the north. In northern Alberta, the boundaries between velocity anomalies are relatively well resolved though appear to be less sharp compared to those from the south. Farther north (above 58° N), the resolution drops significantly and quickly becomes too low to differentiate the velocity variations. On the depth profiles (Figure S4 (e-h)), the output structures are smeared obliquely along the ray propagating direction. The velocity anomalies are recovered reasonably well at depths above 400 km in northern Alberta.

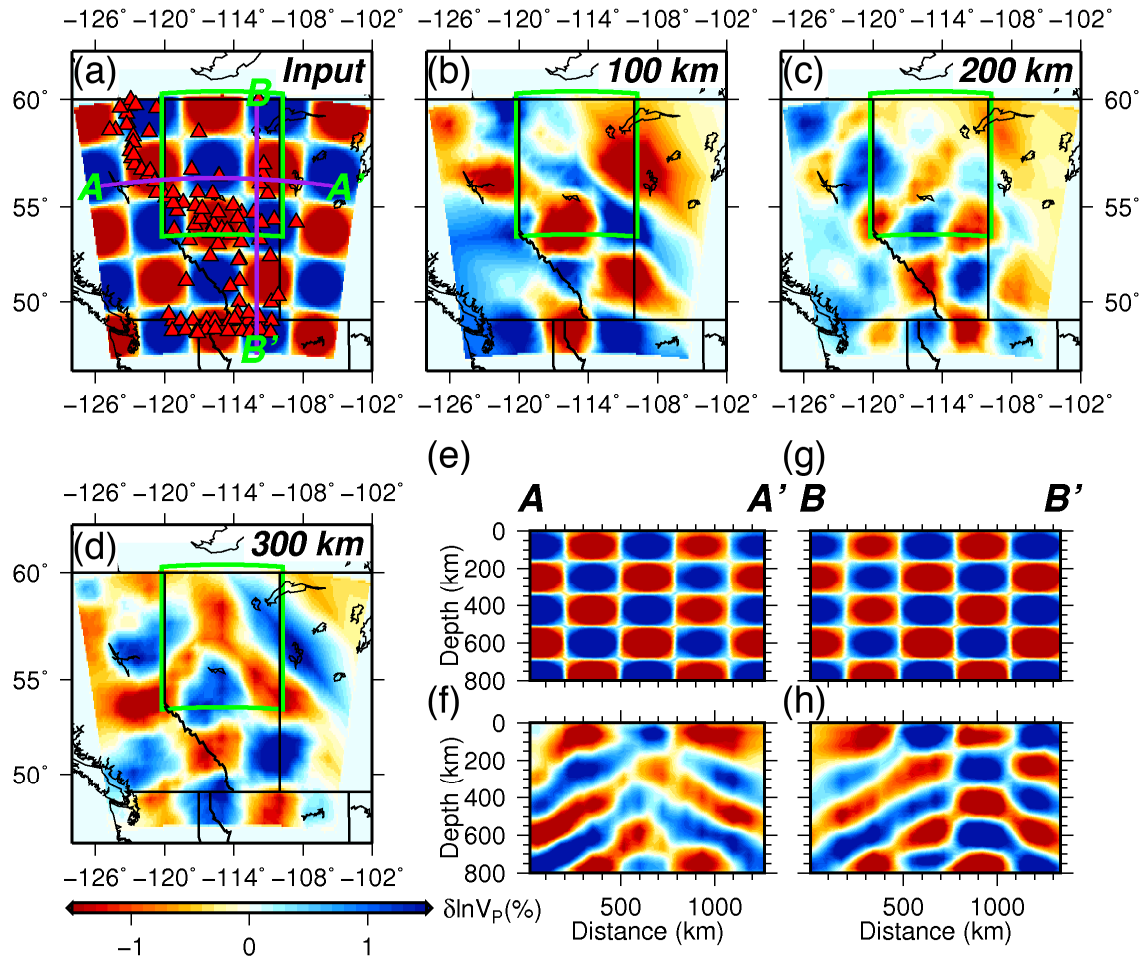


Figure S4. Checkerboard resolution test. (a) Input structures at 100 km depth. The purple lines show the location of two profiles shown in (e) and (g). The study region of Northern Alberta Kimberlite Province is enclosed by the blue rectangle. (b)-(d) Output structures between 100-300 km depths. (e) Input and (f) output structures along profile AA'. (g) and (h) The same as (e) and (f) but for profile BB'.

We perform a series of hypothesis tests to examine the resolvability of our data to the major velocity anomalies, particularly those underlying the three kimberlite groups, in northern Alberta. The most pronounced low-velocity anomaly is observed beneath the Birch Mountains (BM) kimberlites with amplitude of about -1.0%. To examine this structure, we include a quasi-cylindrical low-velocity zone extending to 300 km depth in the input model (Figure S5). We assign slightly higher (-2%) amplitudes to account for the damping and smoothing effects in the inversion. The synthetic travel times are computed based on the actual event-station distributions and random travel-time

perturbations with a standard deviation of 0.06 sec are added to simulate the measurement uncertainties. Then these travel times are inverted for velocities using identical sensitivity kernel and damping criteria as those adopted in real data inversion. The differences between the input and output models provides an intuitive assessment of the quality and reliability of tomographic images. The single low-velocity anomaly is well recovered in the output model with a 60% amplitude recovery. The vertical boundaries are well resolved though are less sharp due to lateral smoothing. The lateral smearing effect is more severe in latitudinal (AA' in Figure S5B) than longitudinal directions (CC' in Figure S5B). Along the direction of kimberlite distribution (i.e., NE-SW), the artificial low-velocity structures are generally confined within 50 km lateral distance of the input anomaly (see CC' in Figure S5B).

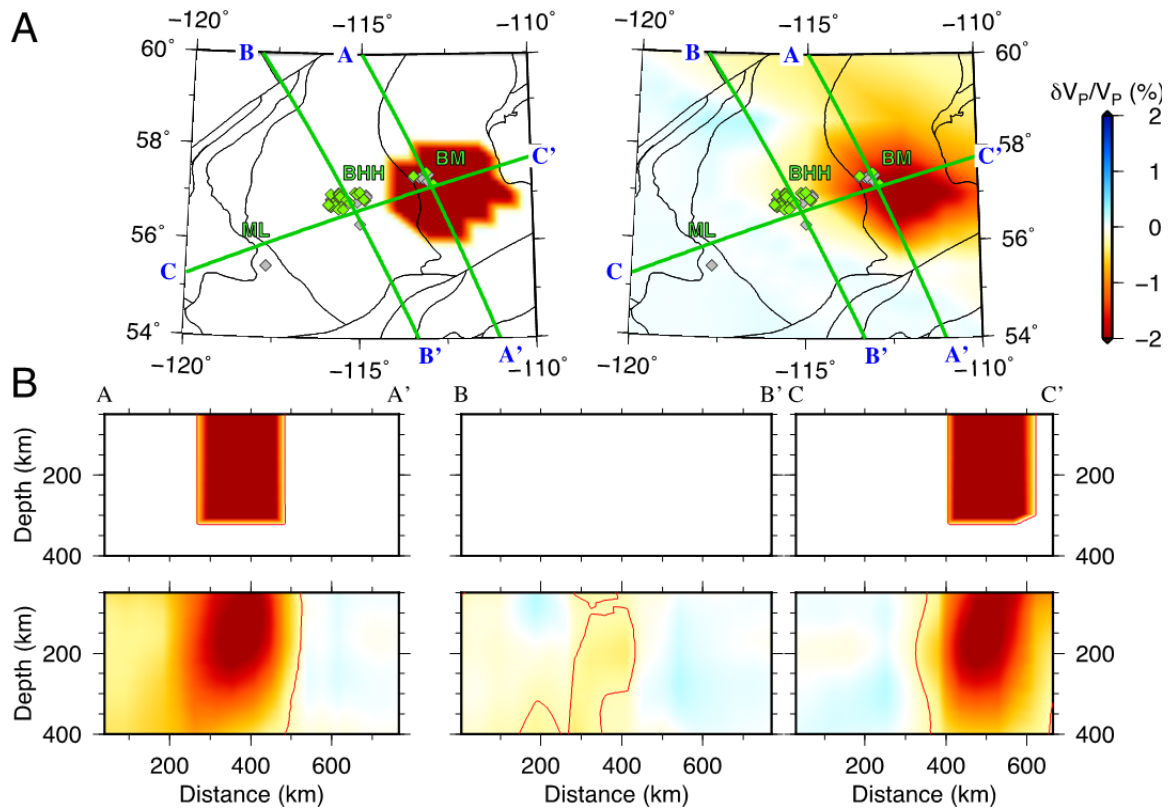


Figure S5. Hypothesis test that examines the sensitivity of data to a low velocity zone beneath the Birch Mountains (BM) kimberlites. A: Input (left) and output (right) models at 100 km depth. B: Three cross-sections showing the input (top) and output (bottom) structures beneath the major kimberlite groups (diamonds). The profile locations are indicated by the green lines in A. The red and blue lines on the cross-sections are -0.5% and 0.5% velocity contours, respectively.

The second model includes an additional low-velocity structure beneath the Mountain Lake (ML) kimberlites (Figure S6A). Its input amplitude (-1%) is half of the low-velocity anomaly underlying the BM kimberlites with a depth extent of 250 km (Figure S6). The inversion is conducted using the same parameters as those used in the first test. The output model recovers the input structures well and resolves two distinctive low-velocity centers (Figure S6A). However, both anomalies are smeared towards the center and, as a result, their separation distance reduces to about half of the input at 200 km depth. The region directly beneath the Buffalo Head Hills (BHH) kimberlites shows inversion artifacts of weak low velocities (BB' in Figure S6B).

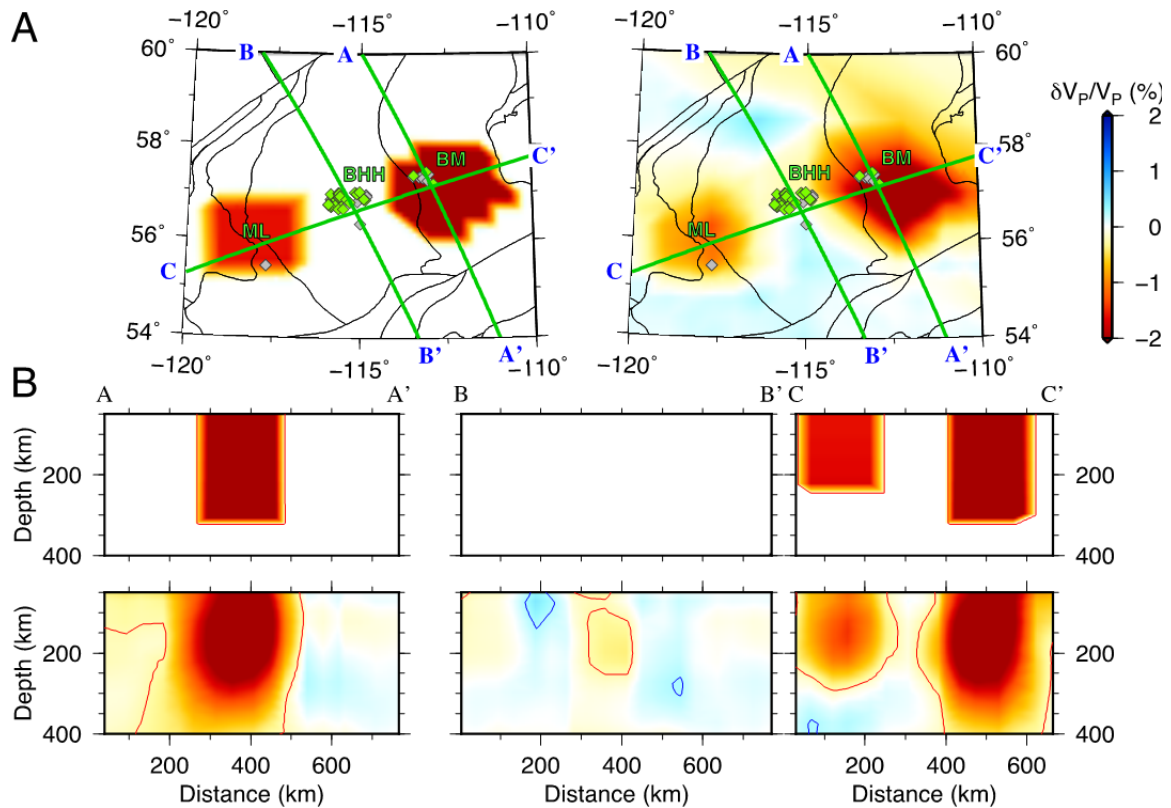


Figure S6. Hypothesis test that examines the sensitivity of data to a low velocity zone beneath the Mountain Lake and Birch Mountains kimberlites. See Figure S2 captions for details.

In the final test, we insert a high-velocity (2%) structure with a vertical extent of 250 km between the two low-velocity anomalies, which resembles the lithosphere beneath the BHH kimberlites. All three input structures are satisfactorily resolved in the output model (Figure S7A). Compared to the second test, the vertical boundaries of the low-velocity anomalies are better constrained due to sharp contrasts with the bounding high-velocity structure (CC' in Figure S7B). On the other hand, the vertical extent of the high-

velocity anomaly is poorly constrained by the data and severely smeared along the ray propagation direction to depth of 350 km (BB' in Figure S7B), suggesting higher data sensitive to lateral velocity variations than those in the vertical direction.

One of the most critical observations in our study is the low-velocity corridor beneath the three kimberlite groups. In the test results, we observe minimal (<50 km) smearing along the strike of kimberlite distribution. The shape of the low-velocity anomalies is well constrained in the presence of a central high-velocity structure. More importantly, the deep continuous low-velocity corridor is not observed in any of the test results, which suggests this structure is not arise from inversion artifact and is a robust feature required by the data.

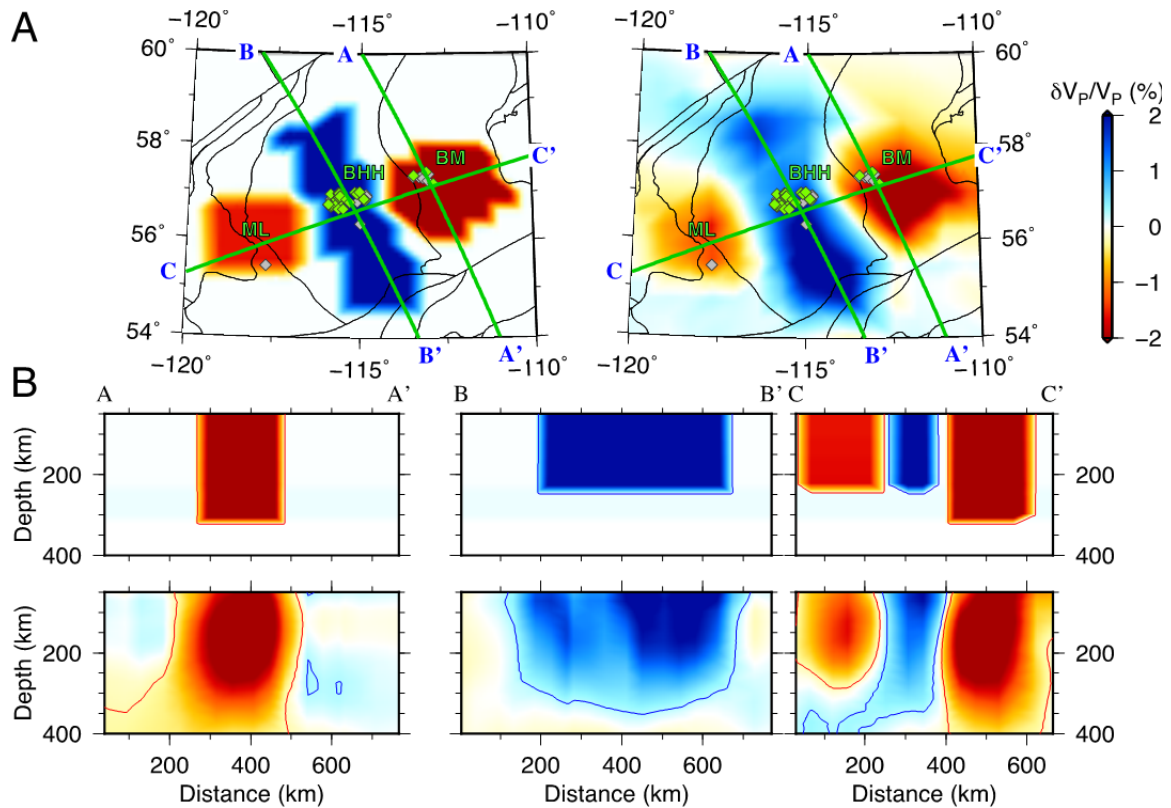


Figure S7. Hypothesis test that examines the sensitivity of data to a low velocity zone beneath the Mountain Lake (ML) and Birch Mountains (BM) kimberlites and high velocity structure beneath the Buffalo Head Hills (BHH) kimberlites. See Figure S2 captions for details.

Text S3. Plate motion rate calculation

We estimate the absolute motion rate of northern Alberta using Euler rotation parameters from five absolute plate motion models. Specifically, the Matthews et al. [Matthews et al., 2016] model combines a post-140 Ma hotspot frame and a pre-140 Ma paleomagnetic

frame of Torsvik et al. [Torsvik et al., 2012]. The Mitchell et al. [Mitchell et al., 2012] model is derived from the paleomagnetic frame of Torsvik et al. [2008] and further paleolongitudinally calibrated using their true polar wander (the motion of the mantle relative to Earth's spin axis) estimates. The subduction reference model of van der Meer et al. [Van Der Meer et al., 2010] is also built on the paleomagnetic frame of Torsvik et al. [Torsvik et al., 2008] but paleolongitudinally calibrated using tomographic images of subducting slabs distributed in the mantle. The Torsvik et al. [Torsvik et al., 2012] model is comprised of a post-130 Ma global moving hotspot frame [O'Neill et al., 2005] and a pre-130 Ma paleomagnetic frame. The Wu et al. [Wu et al., 2017] model calculates Euler reconstruction parameters from the post-260 Ma Baltican apparent polar path of Torsvik et al. [Torsvik et al., 2012]. All the plate motion models in North American coordinates are rotated into the mantle frame using the post-180 Ma plate circuits from Matthews et al. [Matthews et al., 2016].

Text S4. Kimberlite emplacement age

We summarize the previously reported kimberlite ages of northern Alberta in Table S1, which also contains a new U-Pb perovskite date of 90.3 ± 2.6 Ma obtained for the Mountain Lake South intrusion. This U-Pb perovskite date indicates that the Mountain Lake intrusions are the oldest known ultrabasic intrusions in northern Alberta, which is slightly older than but almost within the uncertainty of a previous estimate for the Mountain Lake South body (78 ± 9 Ma) based on apatite fission track dating [Leckie et al., 1997]. The northern Alberta kimberlites (and related rocks) were emplaced during an ~30 m.y. period between 90 and 60 Ma. They are slightly younger than 115-92 Ma kimberlite fields within the North American mid-Cretaceous corridor [Kjarsgaard et al., 2017], and older than the Montana alkaline province intrusions (Sweet Grass Hills minettes; ~50 Ma) [Buhlmann et al., 2000]. The majority of kimberlites occur within the BHH cluster and were emplaced during two intervals at 88-81 Ma (n=10) and 68-60 Ma (n=4; Table S1); the older intrusions are diamondiferous (Table S1). The BM kimberlites were emplaced between 79-70 Ma (n=6; Table S1). Excluding the younger (<70 Ma) BHH kimberlites, which we interpret to have a separate origin, a striking feature of the northern Alberta kimberlite emplacement history is the general eastward younging corridor of the oldest kimberlite intrusions in each cluster.

Table S1. Summary of Northern Alberta Kimberlite Dates

Pipe	Field	Longitude ^t	Latitude ^t	MDC ^t	Age (Ma)	Age Error 2 σ	Method	Mineral	References
Dragon	Birch Mountains	-113.478	57.338		72.4	0.9	Rb-Sr	Phlogopite	1
Phoenix	Birch Mountains	-113.460	57.370	3	70.9	0.4	Rb-Sr	Phlogopite	1
Phoenix	Birch Mountains	-113.460	57.370	3	70.3	1.6	U-Pb	Perovskite	2
Valkyrie	Birch Mountains	-113.286	57.323		75.8	2.7	U-Pb	Perovskite	1
Kendu	Birch Mountains	-113.182	57.307		79.4	1.6	U-Pb	Rutile	3
Xena	Birch Mountains	-113.041	57.254		72.6	2.1	Rb-Sr	Phlogopite	1
Legend	Birch Mountains	-112.883	57.196	4	77.6	0.8	Rb-Sr	Phlogopite	1
K1A	Buffalo Head Hills	-115.864	56.704	2	59.6	2.8	Rb-Sr	Phlogopite	4
K19	Buffalo Head Hills	-115.773	56.742	7	60.3	0.8	Rb-Sr	Phlogopite	4
K91	Buffalo Head Hills	-115.653	56.992	180	86.1	3.0	U-Pb	Perovskite	4
K5A	Buffalo Head Hills	-115.646	56.894	150	87.6	4.6	U-Pb	Perovskite	4,5,6,8
K5B	Buffalo Head Hills	-115.641	56.896	76	87.0	3.0	U-Pb	Perovskite	10
K14B	Buffalo Head Hills	-115.638	56.976	145	86.0	11.0	Rb-Sr	Phlogopite	9
K14A	Buffalo Head Hills	-115.636	56.974	1596	86.8	2.1	U-Pb	Perovskite	4,5,6,8
K7A	Buffalo Head Hills	-115.632	56.939		85.6	2.4	U-Pb	Perovskite	4,5,6,8
K252	Buffalo Head Hills	-115.608	56.920	101	81.3	2.3	Rb-Sr	Phlogopite	4
K11	Buffalo Head Hills	-115.029	57.011	191	84.8	0.9	Rb-Sr	Phlogopite	4
LL08	Buffalo Head Hills	-114.870	56.843	1	86.0	1.2	Rb-Sr	Phlogopite	4
BH225	Buffalo Head Hills	-115.641	56.979		68.4	5.2	U-Pb	Perovskite	4
BH229	Buffalo Head Hills	-115.709	56.856		83.3	5.4	Rb-Sr	Phlogopite	4
BM2	Buffalo Head Hills	-114.826	56.915		63.5	0.7	U-Pb	Perovskite	4
Mountain Lake	Mountain Lake North	-117.717	55.459		72	7	Fission Track	Apatite	7
Mountain Lake	Mountain Lake South	-117.715	55.454		78	9	Fission Track	Apatite	7
DDH-ML-95-3	Mountain Lake South	-117.715	55.454		90.3	2.6	U-Pb	Perovskite	This Study

^tInformation from Faure (2010); MDC=micro-diamond count

References: 1-Aravanis (1999); 2-Eccles et al. (2003); 3-Eccles et al. (2004); 4-Eccles et al. (2008); 5-Carlson et al. (1999); 6-Skeleton et al. (2003); 7-Leckie et al. (1997); 8-Heaman et al. (2004); 9-Eccles et al. (2009); 10-Skeleton and Bursey (1999)

References

- Buhlmann, A., Cavell, P., Burwash, R., Creaser, R., & Luth, R. (2000). Minette bodies and cognate mica-clinopyroxenite xenoliths from the Milk River area, southern Alberta: Records of a complex history of the northernmost part of the Archean Wyoming craton. *Canadian Journal of Earth Sciences*, *37*, 1629–1650. <https://doi.org/10.1139/e00-058>
- Chen, Y., Gu, Y. J., & Hung, S. H. (2018). A New Appraisal of Lithospheric Structures of the Cordillera-Craton Boundary Region in Western Canada. *Tectonics*. <https://doi.org/10.1029/2018TC004956>
- Dahlen, F. A., Hung, S.-H., & Nolet, G. (2000). Fréchet kernels for finite-frequency traveltimes-I. Theory. *Geophysical Journal International*, *141*(1), 157–174. <https://doi.org/10.1046/j.1365-246X.2000.00070.x>
- Hung, S.-H., Dahlen, F. A., & Nolet, G. (2000). Fréchet kernels for finite-frequency traveltimes-II. Examples. *Geophysical Journal International*, *141*(1), 175–203.
- Hung, S.-H., Shen, Y., & Chiao, L. Y. (2004). Imaging seismic velocity structure beneath the Iceland hot spot: A finite frequency approach. *Journal of Geophysical Research B: Solid Earth*, *109*(8), 1–16. <https://doi.org/10.1029/2003JB002889>
- Hung, S.-H., Chen, W. P., Chiao, L. Y., & Tseng, T. L. (2010). First multi-scale, finite-frequency tomography illuminates 3-D anatomy of the Tibetan Plateau. *Geophysical Research Letters*, *37*(6), 1–5. <https://doi.org/10.1029/2009GL041875>
- Kennett, B. L. N., Engdahl, E. R., & Buland, R. (1995). Constraints on seismic velocities in the Earth from traveltimes. *Geophysical Journal International*, *122*(1), 108–124.
- Kjarsgaard, B. A., Heaman, L. M., Sarkar, C., & Pearson, D. G. (2017). The North America mid-Cretaceous kimberlite corridor: Wet, edge-driven decompression melting of an OIB-type deep mantle source. *Geochemistry, Geophysics, Geosystems*. <https://doi.org/10.1002/2016GC006761>
- Leckie, D. A., Kjarsgaard, B. A., Bloch, J., McIntyre, D., McNeil, D., Stasiuk, L., & Heaman, L. (1997). Emplacement and reworking of Cretaceous, diamond-bearing, crater facies kimberlite of central Saskatchewan, Canada. *Geological Society of America Bulletin*, *109*(8), 1000–1020.
- Matthews, K. J., Maloney, K. T., Zahirovic, S., Williams, S. E., Seton, M., & Müller, R. D. (2016). Global plate boundary evolution and kinematics since the late Paleozoic. *Global and Planetary Change*. <https://doi.org/10.1016/j.gloplacha.2016.10.002>
- Van Der Meer, D. G., Spakman, W., Van Hinsbergen, D. J. J., Amaru, M. L., & Torsvik, T. H. (2010). Towards absolute plate motions constrained by lower-mantle slab remnants. *Nature Geoscience*, *3*(1), 36.
- Mitchell, R. N., Kilian, T. M., & Evans, D. A. D. (2012). Supercontinent cycles and the calculation of absolute palaeolongitude in deep time. *Nature*. <https://doi.org/10.1038/nature10800>
- Montelli, R., Nolet, G., Dahlen, F. A., Masters, G., Engdahl, E. R., & Hung, S.-H. (2004). Finite-Frequency Tomography Reveals a Variety of Plumes in the Mantle. *Science*, *303*(5656), 338–343. <https://doi.org/10.1126/science.1092485>
- O'Neill, C., Müller, D., & Steinberger, B. (2005). On the uncertainties in hot spot reconstructions and the significance of moving hot spot reference frames. *Geochemistry, Geophysics, Geosystems*. <https://doi.org/10.1029/2004GC000784>
- Paige, C. C., & Saunders, M. A. (1982). LSQR: An Algorithm for Sparse Linear Equations and

- Sparse Least Squares. *ACM Transactions on Mathematical Software (TOMS)*.
<https://doi.org/10.1145/355984.355989>
- Torsvik, T. H., Müller, R. D., Van der Voo, R., Steinberger, B., & Gaina, C. (2008). Global plate motion frames: toward a unified model. *Reviews of Geophysics*, 46(3).
- Torsvik, T. H., Van der Voo, R., Preeden, U., Mac Niocaill, C., Steinberger, B., Doubrovine, P. V., et al. (2012). Phanerozoic Polar Wander, Palaeogeography and Dynamics. *Earth-Science Reviews*. <https://doi.org/10.1016/j.earscirev.2012.06.007>
- VanDecar, J. C., & Crosson, R. S. (1990). Determination of teleseismic relative phase arrival times using multi-channel cross-correlation and least squares. *Bulletin of the Seismological Society of America*, 80(1), 150–169.
- Wu, L., Kravchinsky, V. A., Gu, Y. J., & Potter, D. K. (2017). Absolute reconstruction of the closing of the Mongol-Okhotsk Ocean in the Mesozoic elucidates the genesis of the slab geometry underneath Eurasia. *Journal of Geophysical Research: Solid Earth*.
<https://doi.org/10.1002/2017JB014261>